Supporting Information

Tetra- and Heptametallic Ru(II),Rh(III) Supramolecular Hydrogen Production Photocatalysts

Gerald F Manbeck,*,[†] Etsuko Fujita,[†] and Karen J Brewer[‡,§]

[†] Chemistry Division, Brookhaven National Laboratory, Upton, NY 11973, USA

[‡] Department of Chemistry, Virginia Tech, Blacksburg, VA 24061, USA

Contents

Table S1. Electrochemical data. S2

Figure S1. Scan rate dependent electrochemical data. S3

Figure S2. CV data after bulk electrolysis. S4

Table S2. Summary of electronic absorption data. S5

Figures S3-S7. UV-vis spectral changes during chemical reduction of $[(bpy)_2Ru(dpp)Ru(bpy)_2]^{4+}$, $[\{(bpy)_2Ru(dpp)\}_2Ru(dpp)]]^{6+}$, $[\{(bpy)_2Ru(dpp)\}_2Ru(dpp)RhCl_2(bpy)]^{7+}$, and $[Rh(dpp)_2Cl_2]^+$ with Na/Hg. S5-9

Figures S8-S10. Spectral changes observed during photochemical reduction of $[\{(bpy)_2Ru(dpp)\}_2Ru(dpp)]]^{6+}$, $[\{(bpy)_2Ru(dpp)\}_2Ru(dpp)RhCl_2(bpy)]^{7+}$, and $[[\{(bpy)_2Ru(dpp)\}_2Ru(dpp)]_2RhCl_2]^{13+}$. S10-11

Figure S11. Excited state transient absorption spectra of $[\{(bpy)_2Ru(dpp)\}_2Ru(dpp)]]^{6+}$, $[\{(bpy)_2Ru(dpp)\}_2Ru(dpp)RhCl_2(bpy)]^{7+}$, and $[[\{(bpy)_2Ru(dpp)\}_2Ru(dpp)]_2RhCl_2]^{13+}$ at various time delays. S12

Figure S12. Residuals to the decay of transient absorption signals at 560 nm for $[\{(bpy)_2Ru(dpp)\}_2Ru(dpp)]^{6+}$, $[\{(bpy)_2Ru(dpp)\}_2Ru(dpp)RhCl_2(bpy)]^{7+}$, and $[[\{(bpy)_2Ru(dpp)\}_2Ru(dpp)]_2RhCl_2]^{13+}$. S13

Figure S13. Decay of the transient signal at 380 nm for $[[\{(bpy)_2Ru(dpp)\}_2Ru(dpp)]_2RhCl_2]^{13+}$ and residuals to the single exponential fit. S14

Figure S14. Normalized excitation spectra for $[\{(bpy)_2Ru(dpp)\}_2Ru(dpp)]^{6+}$ and $[[\{(bpy)_2Ru(dpp)\}_2Ru(dpp)]_2RhCl_2]^{13+}$. S14

Table S1. Electrochemical data. [a]

Complex	$E_{1/2}$ (V)	Assignment
$[\{(bpy)_2Ru(dpp)\}_2Ru(\mathbf{dpp})]^{6+}$	1.56	$2Ru^{III/II}$
	−0.48	$dpp^{0/-}$
	−0.62	$dpp^{0/-}$
	−1.05	$\mathbf{dpp}^{0/-}$
	−1.17	$dpp^{-/2-}$
	−1.32	$dpp^{-/2-}$
	−1.45	$\mathbf{dpp}^{-/2-}$
$[\{(bpy)_2Ru(dpp)\}_2Ru(\mathbf{dpp})RhCl_2(bpy)]^{7+}$	1.59	$2Ru^{III/II}$
	−0.26 [b]	$\mathbf{dpp}^{0/-}$
	−0.49	$dpp^{0/-}$
	ca. −0.55 [b]	$Rh^{III}(\mathbf{dpp}^{-}) + e \rightarrow Rh^{I}(\mathbf{dpp}^{0})$
	−0.62	$dpp^{0/-}$
	−1.04	Rh(I) $\mathbf{dpp}^{0/-}$
	−1.16	$dpp^{-/2-}$
	−1.32	$dpp^{-/2-}$
$[\{(bpy)_2Ru(dpp)\}_2Ru(\mathbf{dpp})]_2RhCl_2]^{13+}$	1.60	$4Ru^{III/II}$
	−0.25 [b]	$Rh^{III/II/I}$
	−0.50	$2dpp^{0/-}$
	−0.62	$2dpp^{0/-}$
	−0.75	Rh(I) $\mathbf{dpp}^{0/-}$
	−1.05	Rh(I) $\mathbf{dpp}^{0/-}$
	−1.18	$2dpp^{-/2-}$
$[\{(bpy)_2Ru(dpp)\}_2RhCl_2]^{5+}$ [c]	1.63	$Ru^{III/II}$
	−0.37	$Rh^{III/II/I}$
	−0.76	Rh(I) $dpp^{0/-}$
	−1.00	Rh(I) $dpp^{0/-}$
$[(bpy)_2Ru(dpp)RhCl_2(phen)]^{3+}$ [d]	1.61	$Ru^{III/II}$
	−0.39	$Rh^{III/II}$
	−0.74 [b]	$Rh^{II/I}$
	−0.98	Rh(I) $dpp^{0/-}$

[a] Voltammograms were recorded in deoxygenated acetonitrile at 293 K with 0.1 M Bu_4NPF_6 as supporting electrolyte. bpy = 2,2′-bipyridyl, dpp = 2,3-bis(2-pyridyl)pyrazine, phen = 1,10-phenanthroline. [b] E_p^c for overlapping or irreversible couples. [c] Elvington, M.; Brewer, K. J. *Inorg. Chem.* **2006**, *45*, 5242. [d] Zigler, D. F.; Wang, J.; Brewer, K. J. *Inorg. Chem.* **2008**, *47*, 11342.

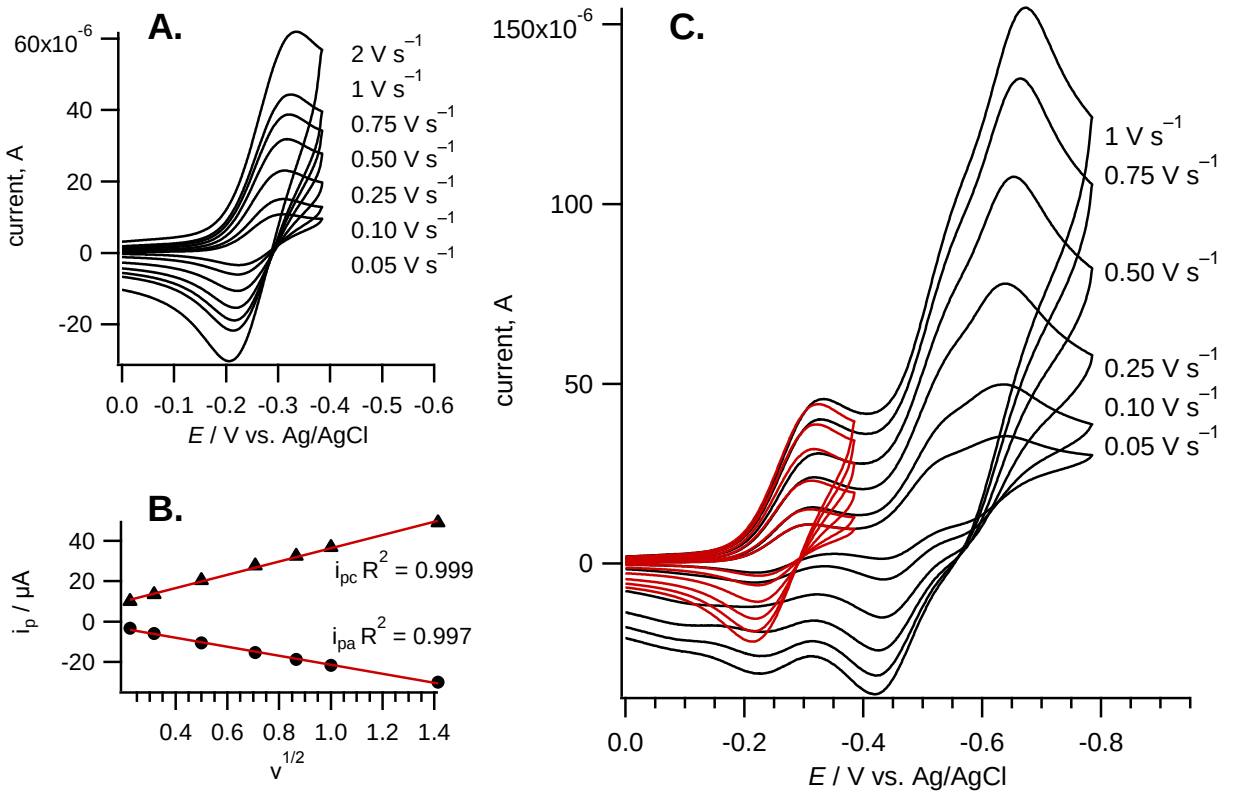

Figure S1. Scan rate dependence for the one-electron reduction (A) and four-electron reduction (C) of **Ru$_3$Rh** $[\{(bpy)_2Ru(dpp)\}_2Ru(dpp)RhCl_2(bpy)]^{7+}$ in CH_3CN with a 100 mV s^{-1} scan rate and 0.1 M Bu_4NPF_6 electrolyte. Plot **B** shows the linear dependence of the cathodic and anodic peak currents on $v^{1/2}$ as expected for a chemically reversible, diffusion-controlled single electron reduction. The anodic peak current was estimated as the absolute current in plot **A** since an accurate baseline at the switching potential was difficult to determine.

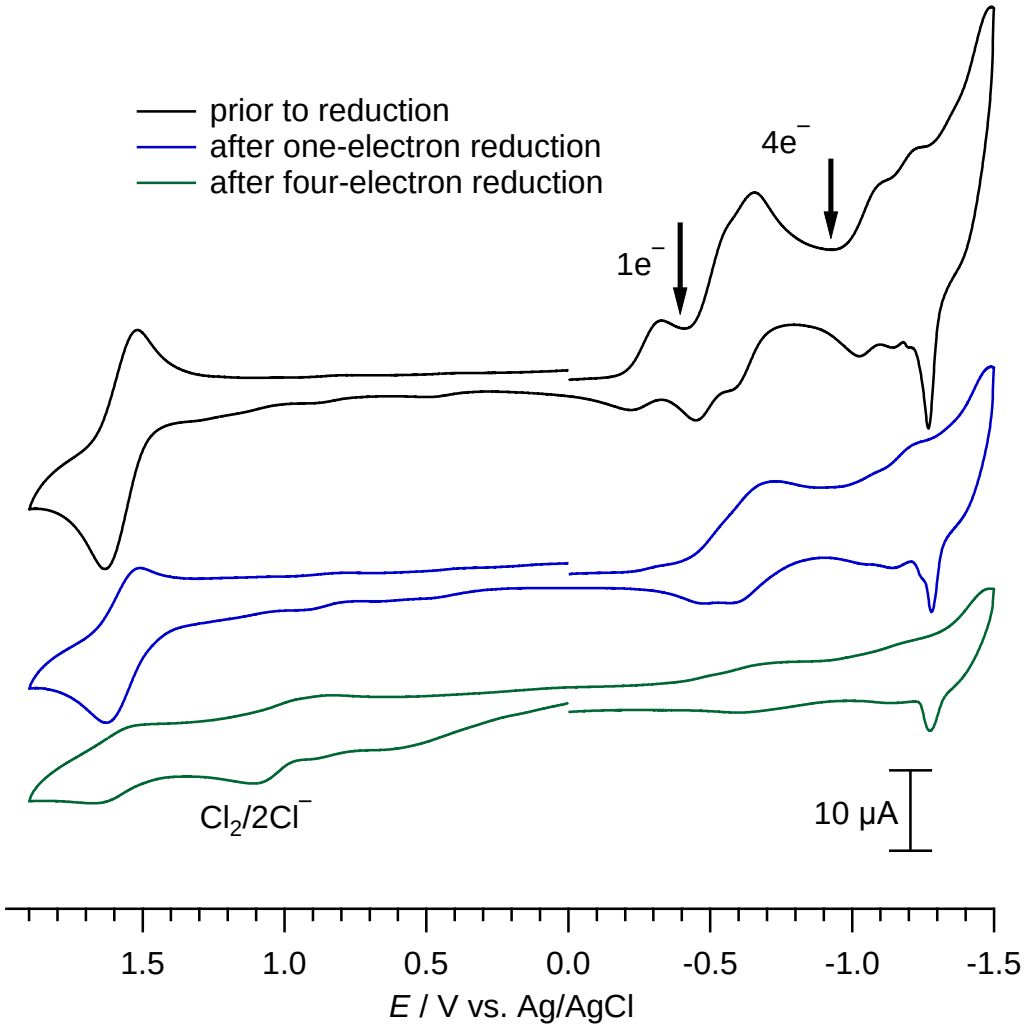

Figure S2. Cyclic voltammetry of **Ru_3Rh** $[\{(bpy)_2Ru(dpp)\}_2Ru(dpp)RhCl_2(bpy)]^{7+}$ before and after bulk electrolysis in CH_3CN for the purposes of coulometry and product analysis. Electrolysis at −370 mV consumed one equivalent of charge and no Cl^- was detected in solution showing that the singly reduced species is a stable dpp-localized radical. In a separate experiment, electrolysis at −900 mV consumed 4 equivalents of charge due to the reduction of Rh(III) to Rh(I) and the reduction of two (μ-Ru,Ru-dpp) ligands. Dissociation of Cl^- was confirmed by its detection upon oxidation.

Table S2. Summary of electronic absorption data. [a]

Complex	λ_{max} (nm)	$\varepsilon \times 10^{-4}$ (M^{-1} cm^{-1})	Major Transitions
$[\{(bpy)_2Ru(dpp)\}_2Ru(dpp)]$ $(PF_6)_6$	281	12.8	bpy π→ π *
	340	5.1	dpp π → π *
	416	2.4	Ru(d π)→bpy(π *) CT
	540	4.0	Ru(d π)→dpp(π *) CT
$[\{(bpy)_2Ru(dpp)\}_2Ru(dpp)RhCl_2(bpy)]$ $(PF_6)_7$	281	11.6	bpy π → π *
	341	5.7	dpp π → π *, Rh(d π)→dpp(π *) CT
	416	2.2	Ru(d π)→bpy(π *) CT
	534	4.0	Ru(d π)→dpp(π *) CT
$[\{(bpy)_2Ru(dpp)\}_2Ru(dpp)]_2RhCl_2$ $(PF_6)_{13}$	281	23.5	bpy π→ π *
	314	12.2	dpp π → π *
	340	11.0	dpp π → π *, Rh(d π)→dpp(π *) CT
	416	4.2	Ru(d π)→bpy(π *) CT
	535	8.0	Ru(d π)→dpp(π *) CT

[a] In acetonitrile. bpy = 2,2′-bipyridyl, dpp = 2,3-bis(2-pyridyl)pyrazine.

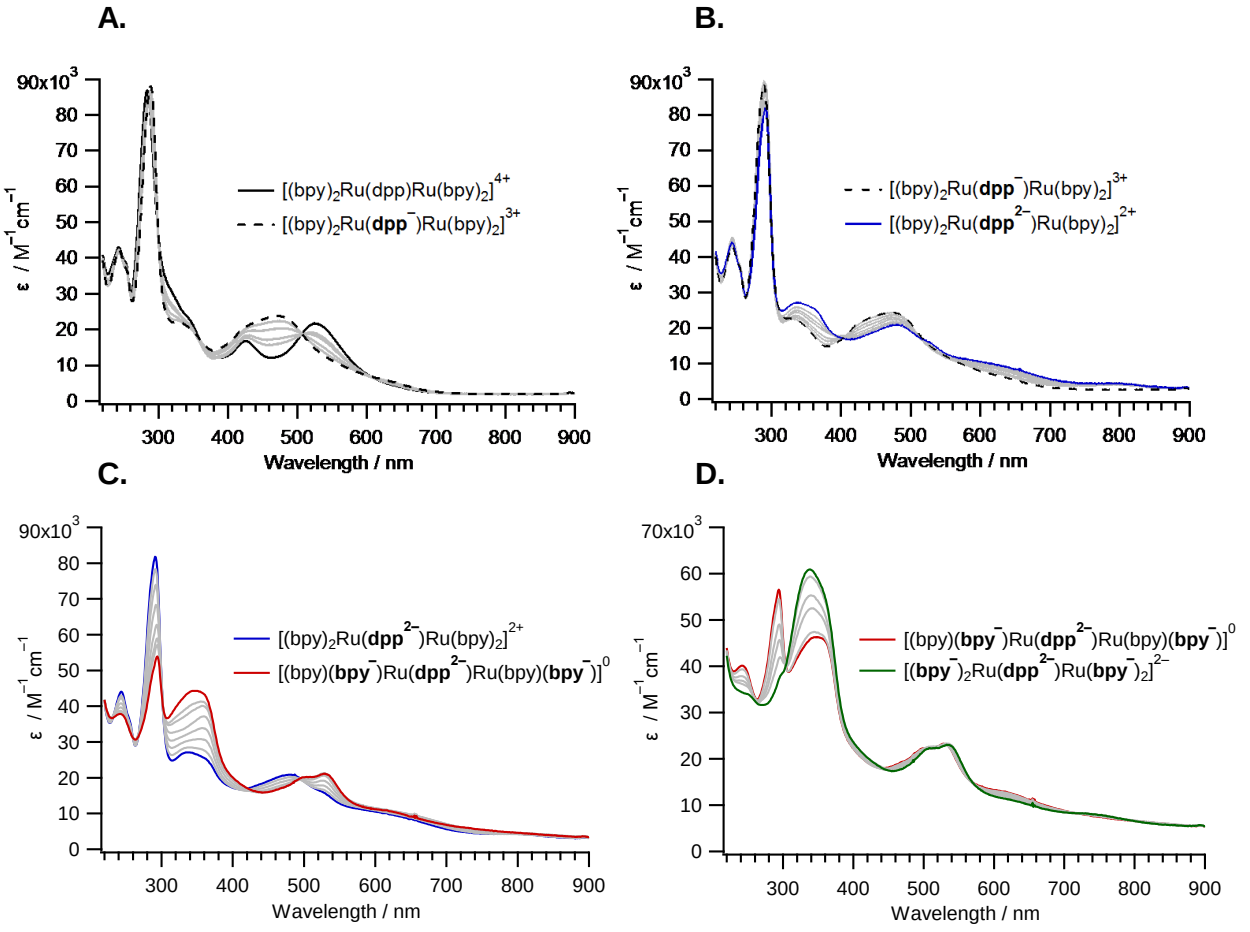

Figure S3. Chemical reduction of $[(bpy)_2Ru(dpp)Ru(bpy)_2]^{4+}$ with sodium amalgam in CH_3CN.

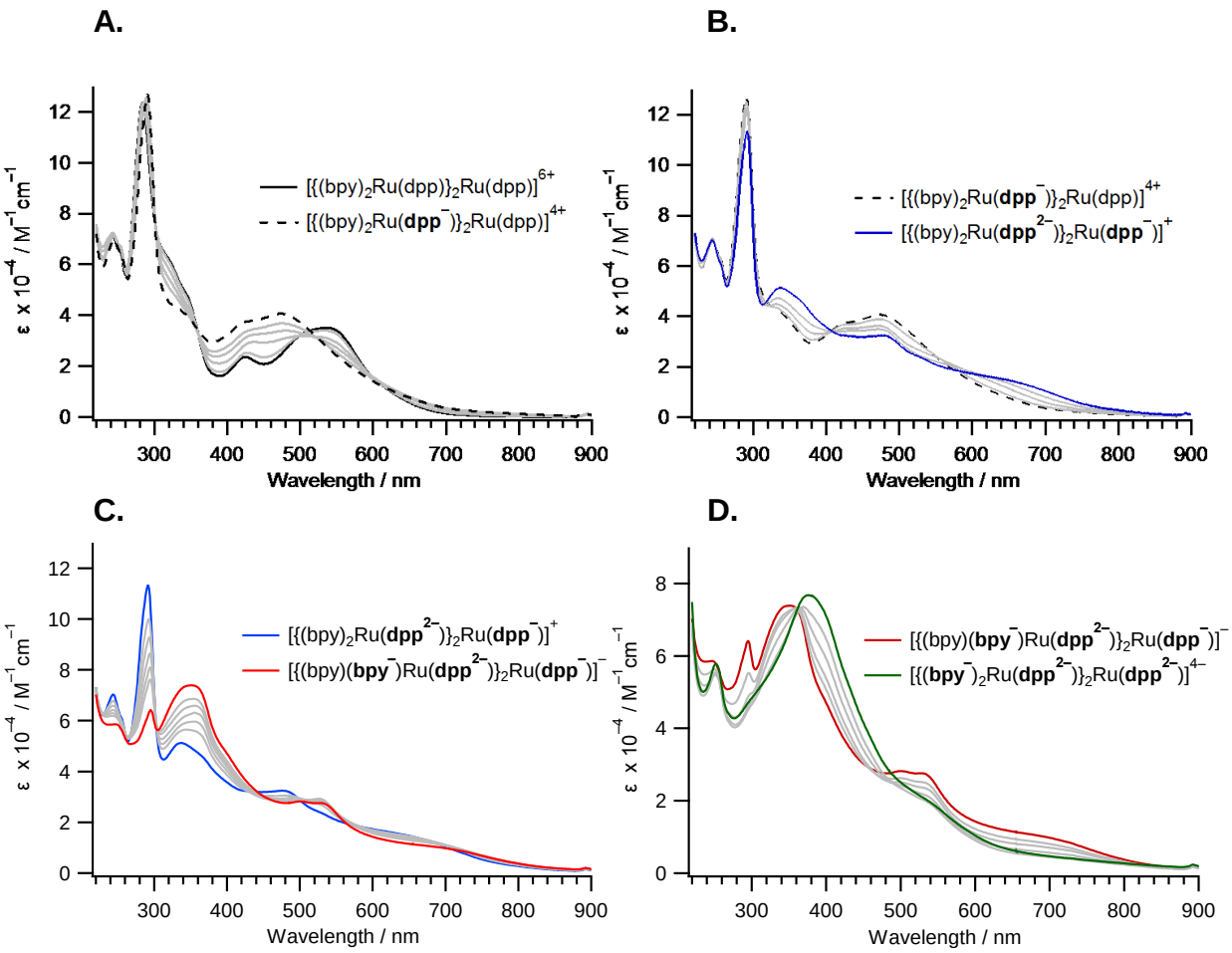

Figure S4. Chemical reduction of $[\{(bpy)_2Ru(dpp)\}_2Ru(dpp)]^{6+}$ with sodium amalgam in CH_3CN.

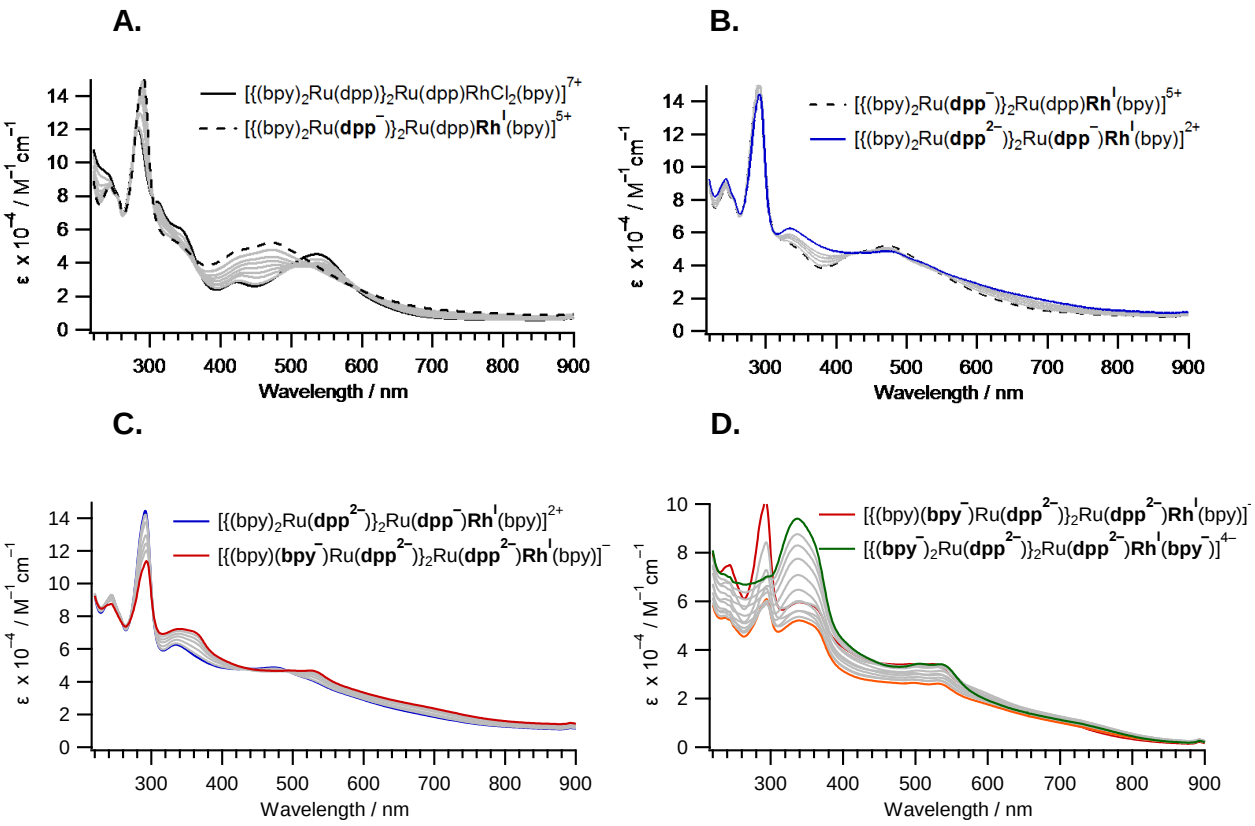

Figure S5. Chemical reduction of $[\{(bpy)_2Ru(dpp)\}_2Ru(dpp)RhCl_2(bpy)]^{7+}$ with sodium amalgam in CH_3CN. In plot D, the decrease in absorptivity at all wavelengths is attributed to insolubility of the neutral complex in acetonitrile, though it appears solubility is improved for anionic species. Due to the solubility problem, extinction coefficients in plot D are assumed as approximate.

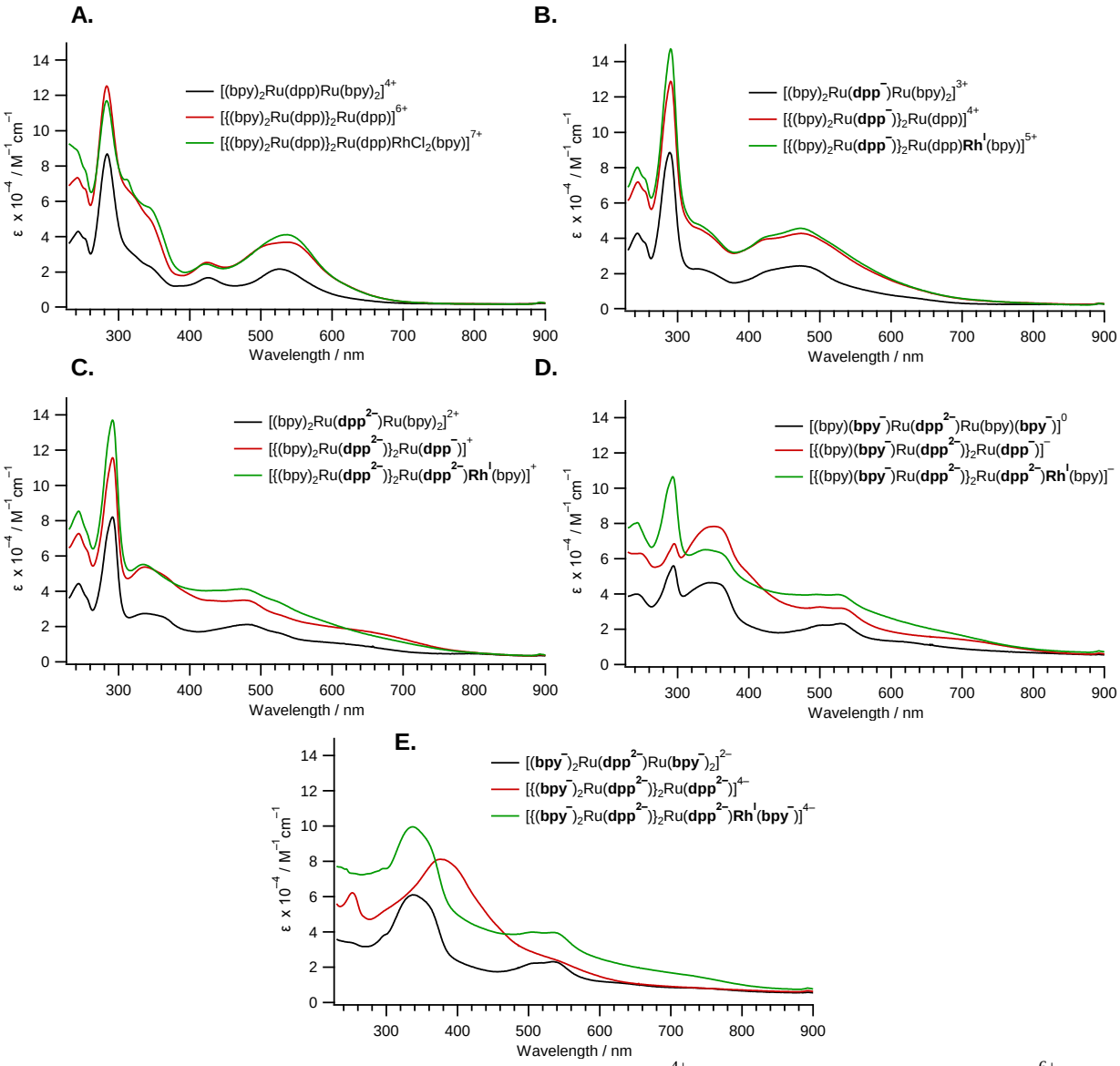

Figure S6. Reduction of $[(bpy)_2Ru(dpp)Ru(bpy)_2]^{4+}$, $[\{(bpy)_2Ru(dpp)\}_2Ru(dpp)]]^{6+}$, and $[\{(bpy)_2Ru(dpp)\}_2Ru(dpp)RhCl_2(bpy)]^{7+}$ with Na/Hg. Each plot shows the reduction stage with greatest similarity for each species.

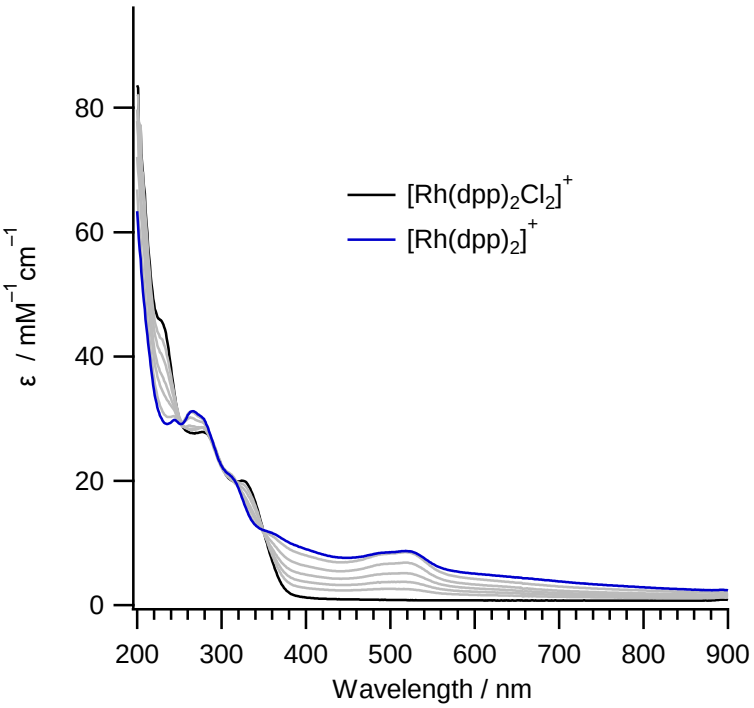

Figure S7. Reduction of $[Rh(dpp)_2Cl_2]PF_6$ with Na/Hg.

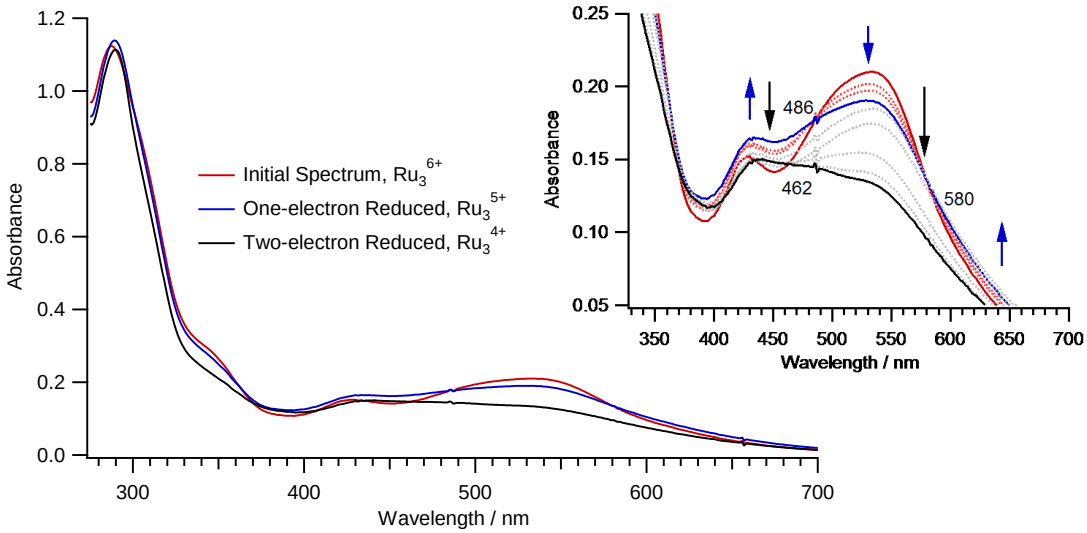

Figure S8. Photo-reduction of $[\{(bpy)_2Ru(dpp)\}_2Ru(dpp)]^{6+}$ in CH_3CN using *N*,*N*-dimethylaniline as the reductant. The inset shows an expansion of the low energy λ_{max}. Both $1e^-$ and $2e^-$ reduction were were characterized by diminished intensity of the 540 nm absorbance but were distinguishable by an initial increase in absorptivity at 433 nm and for $\lambda > 580$ nm with clear isosbestic points (red to blue) followed by the second step in which absorptivity decreased for all $\lambda > 300$ nm (blue to black).

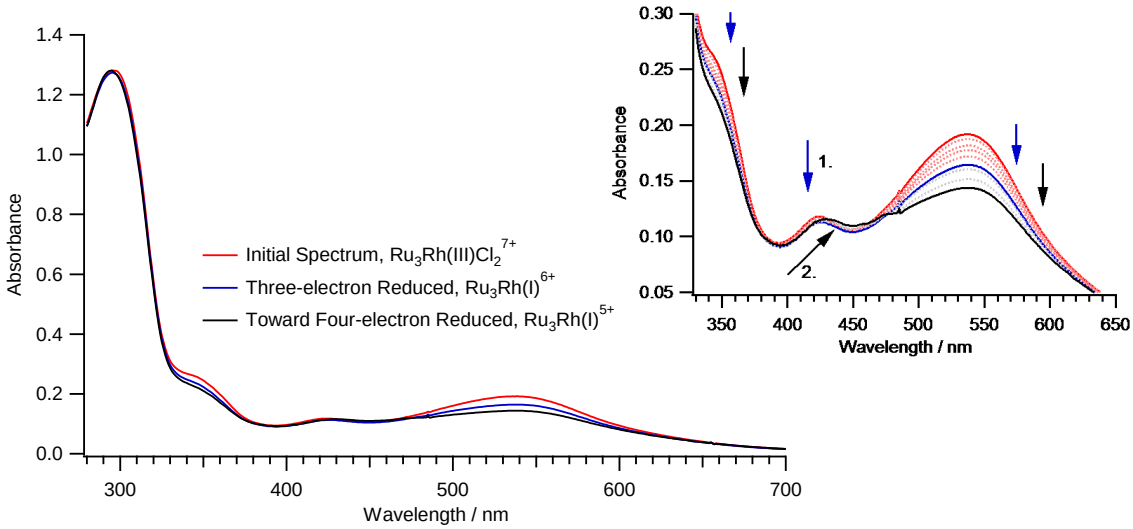

Figure S9. Photo-reduction of $[\{(bpy)_2Ru(dpp)\}_2Ru(dpp)RhCl_2(bpy)]^{7+}$ in CH_3CN using *N*,*N*-dimethylaniline as the reductant. The first spectral changes include a slight red shift of the 422 nm absorbance and a decrease in absorbance of the low energy MLCT band with $\lambda_{max} = 536$ nm. This process corresponds to the reduction of a μ-Ru,Ru-dpp bridging ligand as in Ru_3 above; however, the 3-fold decrease in quantum yield is attributed to the reduction of Rh(III) to Rh(I) for a total of three reductions. During the second series of spectral changes, an isosbestic point is observed at 476 nm and the low energy band continues to decrease. This change is attributed to reduction of the second μ-Ru,Ru-dpp bridging ligand.

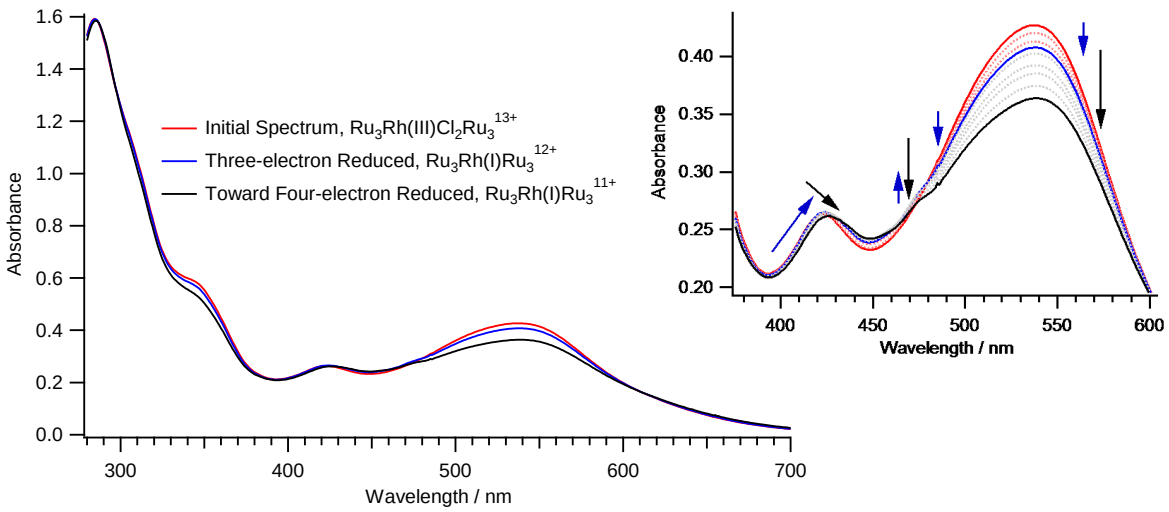

Figure S10. Photo-reduction of $[[\{(bpy)_2Ru(dpp)\}_2Ru(dpp)]_2RhCl_2]^{13+}$ in CH_3CN using *N*,*N*-dimethylaniline as the reductant. The first spectral changes include isosbestic points at 419 and 480 nm and a decrease in the low energy MLCT band with λ_{max} = 536 nm. This process corresponds to the reduction of a μ-Ru,Ru-dpp bridging ligand as in Ru_3 above; however, the 3-fold decrease in quantum yield is attributed to the reduction of Rh(III) to Rh(I) for a total of three reductions. During the second series of spectral changes, an isosbestic point is observed at 474 nm and the low energy band continues to decrease. This change is attributed to reduction of the second μ-Ru,Ru-dpp bridging ligand.

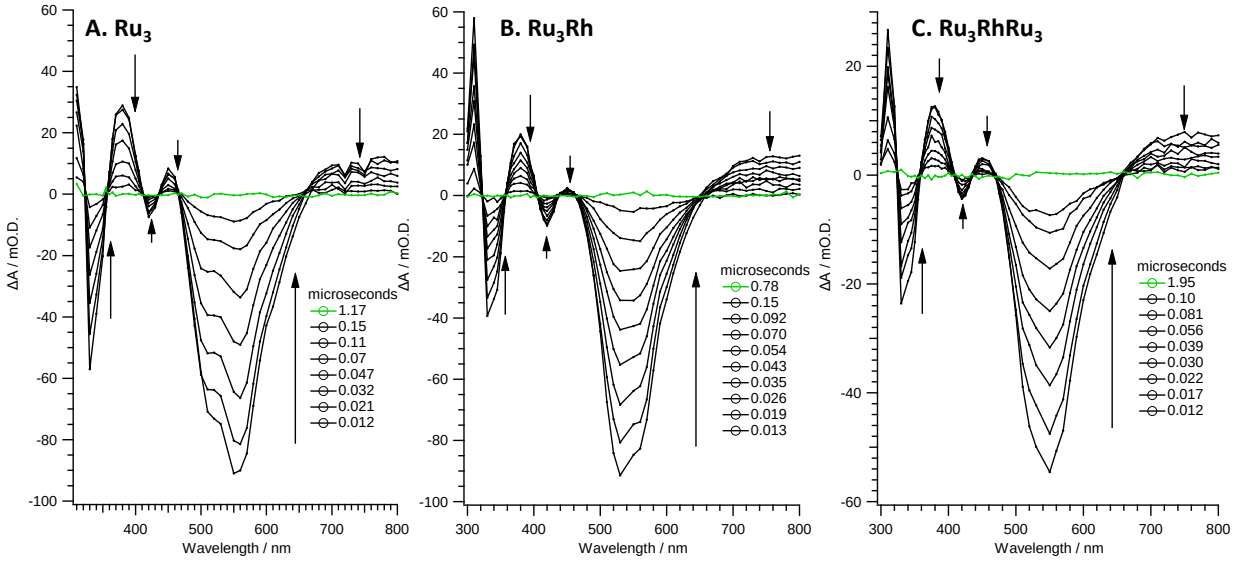

Figure S11. Excited state transient absorption spectra of $[\{(bpy)_2Ru(dpp)\}_2Ru(dpp)]^{6+}$ (A), $[\{(bpy)_2Ru(dpp)\}_2Ru(dpp)RhCl_2(bpy)]^{7+}$ (B), and $[[\{(bpy)_2Ru(dpp)\}_2Ru(dpp)]_2RhCl_2]^{13+}$ (C) in CH_3CN with λ_{exc} = 532 nm.

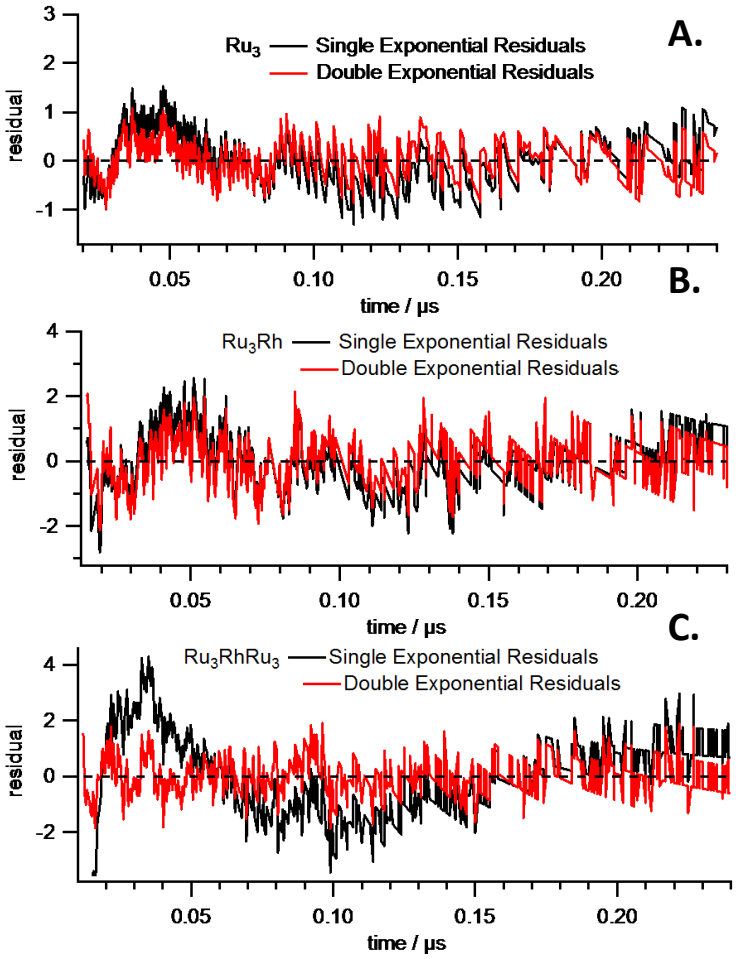

Figure S12. Residuals to the decay of transient absorption signals at 560 nm for $[\{(bpy)_2Ru(dpp)\}_2Ru(dpp)]^{6+}$ (A), $[\{(bpy)_2Ru(dpp)\}_2Ru(dpp)RhCl_2(bpy)]^{7+}$ (B), and $[[\{(bpy)_2Ru(dpp)\}_2Ru(dpp)]_2RhCl_2]^{13+}$ (C). In A and B, single and double exponential decays model the data equally and the single exponential lifetimes are reported. In C, a double exponential fit was needed to model the data. See the Manuscript for lifetimes and discussion.

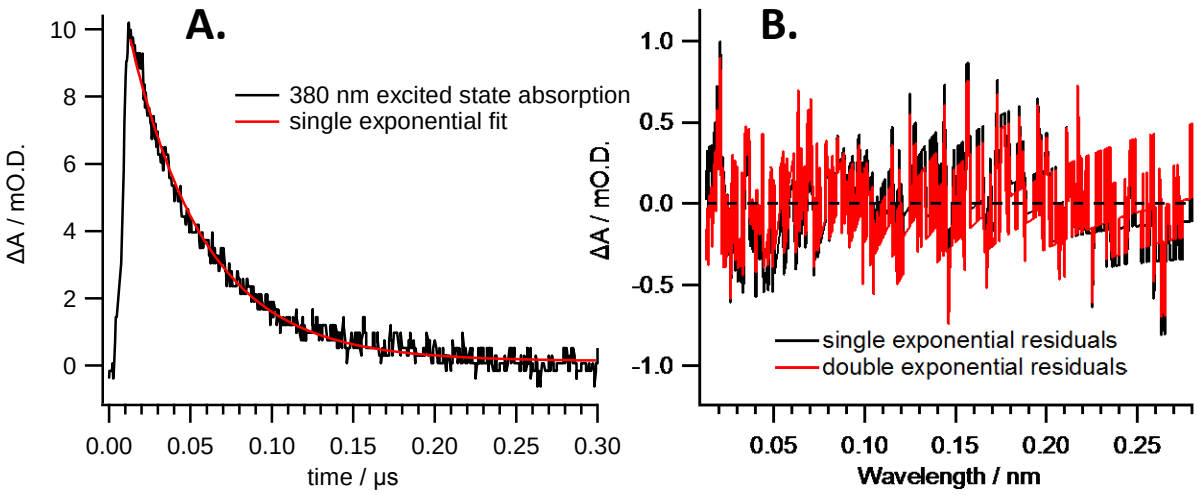

Figure S13. Decay of the transient signal at 380 nm for $[[\{(bpy)_2Ru(dpp)\}_2Ru(dpp)]_2RhCl_2]^{13+}$ fit to a single exponential function (A). The residuals (B) show that the single exponential function is an appropriate model of the data, unlike in Figure S12-C above (560 nm).

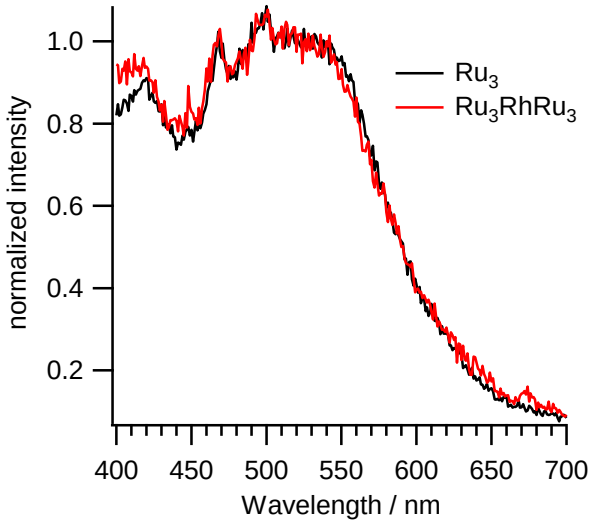

Figure S14. Normalized excitation spectra for $[\{(bpy)_2Ru(dpp)\}_2Ru(dpp)]^{6+}$ and $[[\{(bpy)_2Ru(dpp)\}_2Ru(dpp)]_2RhCl_2]^{13+}$. Identical traces suggest emission of the same excited state origin (^{3}MLCT, Ru→μ-Ru,Ru-dpp).